

Received 18 September 2024, accepted 8 October 2024, date of publication 14 October 2024, date of current version 4 November 2024.

Digital Object Identifier 10.1109/ACCESS.2024.3479272



# High-Efficiency Broadband Infrared Thin-Film Germanium Photodetector Enhanced by a Resonant Cavity and a Nano-Slit Metasurface

CHING-YU HSU<sup>®</sup>1, (Graduate Student Member, IEEE), ZINGWAY PEI<sup>®</sup>2,3, (Senior Member, IEEE), AND JIA-MING LIU<sup>1,2,4</sup>, (Fellow, IEEE)

<sup>1</sup>College of Photonics, National Yang Ming Chiao Tung University, Tainan 711, Taiwan

Corresponding authors: Zingway Pei (zingway@dragon.nchu.edu.tw) and Jia-Ming Liu (liu@ee.ucla.edu)

This work was supported in part by the National Science and Technology Council (NSTC), Taiwan, under Grant NSTC-112-2221-E-005-066- and Grant NSTC-111-2622-E-005-008-; and in part by the Ministry of Education (MOE) in Taiwan "Innovation and Development Center of Sustainable Agriculture" from The Featured Areas Research Center Program within the framework of the Higher Education Sprout Project, and Yushan Scholar Project.

ABSTRACT This paper presents a novel design for high-quantum-efficiency and broadband Ge-on-Si photodetectors. The design entails placing a SiO<sub>2</sub>-filled nano-slit metasurface on a free-standing resonantcavity enhanced (RCE) Ge structure to achieve high quantum efficiency in a broad spectral range of 1000-1600 nm. This design addresses the limitations of narrow resonance linewidths for conventional RCE devices with Fabry-Perot cavities. The SiO<sub>2</sub>-filled metasurface introduces diffraction and additional phase matching of the incident light field to horizontal guided modes, thus enhancing light coupling to the active region at non-resonance wavelengths of the Fabry-Perot mode. The device with this design exhibits an average quantum efficiency of 73.28 % in the 1000-1600 nm spectral range and a minimum quantum efficiency of approximately 60%, which is three times higher than a device without the metasurface structure. The quantum efficiency at around 1300 nm reaches 76.65%, and that at around 1550 nm reaches 98.69%. The estimated responsivity is 0.81 A/W and 1.23 A/W, respectively. For high-speed applications, a device comprising a Si spacer below a thin Ge layer of 600 nm thickness is aimed for operation at a bandwidth of 55 GHz. This device exhibits an average of 64.96% quantum efficiency with a minimum quantum efficiency of around 60%. Its peak quantum efficiency reaches 92.61% at around 1300 nm and 94.65% at around 1550 nm. The corresponding estimated responsivity is 0.98 A/W and 1.18 A/W, respectively. Both designs are innovative solutions for high-speed infrared photodetectors of high quantum efficiency over a broad spectral range.

**INDEX TERMS** Broad-bandwidth photodetectors, Germanium photodetectors, infrared photodetectors, metasurface, resonant-cavity enhancement (RCE).

### I. INTRODUCTION

Germanium photodetectors are suitable for infrared photodetection up to the 1600 nm wavelength [1]. However, conventional Ge photodetectors have a low responsivity beyond the 1550 nm wavelength because the absorption

The associate editor coordinating the review of this manuscript and approving it for publication was Bilal Khawaja.

coefficient of Ge drastically drops at 1550 nm. Photodetectors with a broad infrared spectrum are crucial in applications involving infrared photodetection at different wavelengths. Infrared photodetection is useful in several fields in several fields, such as optical communications [2], [3], [4], light detection and ranging (LiDAR) [5], agriculture [6], and biomedical applications [7]. Conventional optical communication systems operate in a transmission window of

<sup>&</sup>lt;sup>2</sup>Graduate Institute of Optoelectronic Engineering, National Chung Hsing University, Taichung 402, Taiwan

<sup>&</sup>lt;sup>3</sup>Innovative Development Center of Sustainable Agriculture, National Chung Hsing University, Taichung 402, Taiwan

<sup>&</sup>lt;sup>4</sup>Department of Electrical Engineering, University of California at Los Angeles, Los Angeles, CA 90095, USA



1310 nm and 1550 nm by using the dense wavelength division multiplexer (DWDM) technology. DWDM combines several signals of different wavelengths in a narrow wavelength range for transmission through a single fiber to ensure high data transmission capacity. By contrast, the coarse wavelength division multiplexer (CWDM) technique utilizes a broad infrared spectrum [8]. CWDM is typically used in optical I/O and co-package optics for low-loss and high-capacity chip-to-chip data communications. In addition to optical communications, infrared spectra are used in agriculture and chemical verification processes that entail measuring the absorption spectrum of an organic substance [9]. These applications increase the demand for broadband infrared Ge photodetectors.

Ge photodetectors are compatible with silicon-integrated circuits. Various methods are currently available for fabricating high-quality Ge thin film on Si. For example, the two-step Ge epitaxial technique is effective to overcome the 4.2% lattice mismatch between Ge and Si [10]. In this technique, a Ge buffer layer is first deposited on a Si substrate, and then a high-quality Ge layer is grown on the buffer layer through chemical vapor deposition [11], [12] or molecular beam epitaxy [13].

Various types of Ge photodetectors have been developed. Waveguide-type Ge photodetectors realized high speed and high responsivity by edge coupling to a narrow, long waveguide [14], [15]. However, these photodetectors are only suitable for optical communications because their coupling angle into the waveguide structure is limited. Compared with waveguide Ge photodetectors, vertical PIN photodetectors are generally less complex to fabricate, but they have the disadvantage of the trade-off between high speed and high responsivity [16]. In a vertical PIN photodetector, a thick active layer ensures high responsivity at the expense of speed, whereas a thin layer increases the speed at the expense of responsivity. To alleviate this limitation, various innovations, such as light trapping holes [17], [18], guided-mode resonance grating [19], [20], resonant-cavity enhancement (RCE) [21], [22], [23], [24], metasurface [25], and surface plasmonic resonance [26], [27], have been used in vertical PIN photodetectors. In devices with a thin active layer, RCE can substantially improve the quantum efficiency to nearly 100%, with potentially high responsivity and high speed [28].

RCE Ge photodetectors have an absorbing Fabry–Perot cavity in the device. A strong standing wave in the cavity dramatically enhances the absorbance of the device at resonance. However, resonance only occurs at specific discrete wavelengths. At non-resonance wavelengths, RCE Ge photodetectors exhibit relatively low absorbance and, thus low quantum efficiencies. This narrow linewidth of resonance limits the broad-spectrum applications of RCE Ge photodetectors.

Metasurfaces composed of subwavelength structures can manipulate electromagnetic waves across a broad frequency range [29]. By adjusting the geometry of each metaatom, we can design a metasurface to properly control wave properties, including the amplitude and phase of a wave [30]. Recently, metasurfaces have been widely applied in waveform shaping, micro-nano resonators, and enhanced lightmatter interaction [31]. The push for miniaturization of multifunctional devices has influenced fields such as photonics and communications.

In this work, we propose a novel design for a broadbandwidth Ge infrared photodetector consisting of a nanoscale SiO<sub>2</sub>-filled metasurface and a RCE Ge structure. Compared with conventional RCE devices, the device has a broadened spectrum of high quantum efficiency. The absorption spectrum of the device can be tailored by varying the period and the Ge duty factor of the metasurface. We focus on the case where the incident wave is polarized in the direction perpendicular to the periodic direction of the metasurface as shown on the top of Fig. 1. Variations in wave polarization will be discussed in future works. A theoretical bandwidth model of photodetectors is utilized to estimate the speed of the proposed device. To further optimize the speed of the device, devices are designed both with and without a Si spacer for comparison. A device comprising a Si spacer and a thin Ge layer of 600 nm thickness is designed for operation at a bandwidth of 55 GHz with a 3-dB cutoff. Both structures without and with a Si spacer exhibit a broad spectrum of high quantum efficiency (from 1000 nm to 1580 nm) with the RCE mechanism. Overall, our findings indicate that designs combining RCE with properly tailored metasurfaces pave the way for infrared photodetectors that possess both high quantum efficiency and broad bandwidth.

## **II. DEVICE CONCEPT**

The proposed device comprises a free-standing Ge RCE photodetector with a SiO<sub>2</sub>-filled nano-slit metasurface at the top of the detector and a distributed Bragg reflector (DBR) at the bottom as depicted in Fig. 1. The optimization of the free-standing Ge RCE photodetector without a nanoslit metasurface was carried out in our previous work [28]. To ensure total reflection at the interface between the Ge layer and the bottom DBR, a three-period SiO<sub>2</sub>/Si DBR is employed. The Ge metasurface, filled with SiO<sub>2</sub> for passivation, is integrated into the RCE structure. Beneath the metasurface is a Ge base of 100 nm thickness to facilitate light absorption and current extraction. This device structure is suitable for various types of photodetectors. We also develop a device with a Si spacer for comparison with that without a Si spacer. Figure 1(a) shows the structure of a device without a Si spacer, in which the resonant cavity consists of the periodic metasurface and the Ge base. The structure of the device in a single metasurface period is marked within a red dashed square, and its detailed setting is illustrated on the right side of Fig. 1(a). The overall thickness of the Ge layer,  $d_{\text{Ge,homo}}$ , is from the bottom of the Ge base to the top of the metasurface. Figure 1(b) illustrates the structure of a device with a Si spacer, in which the resonant cavity comprises a thin



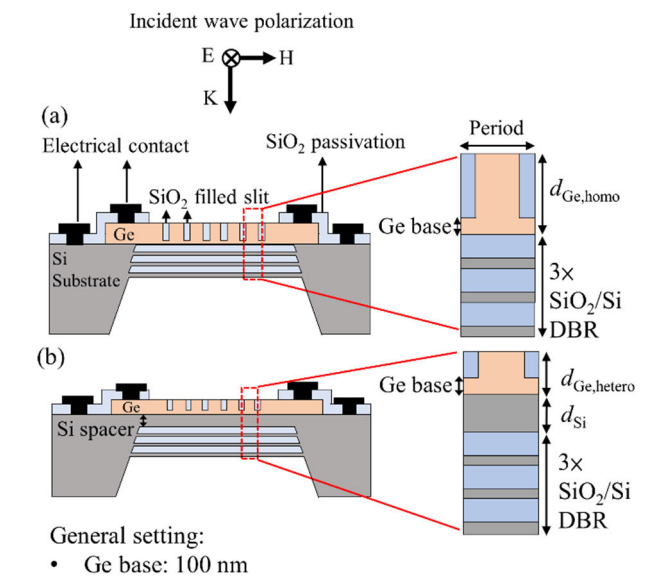


FIGURE 1. Schematics of the devices (a) without a Si spacer (b) and with a Si spacer.

d<sub>Ge,hetero</sub>:100 nm to 900 nm
 d<sub>Si</sub>: 15 nm to 660 nm

DBR thickness: SiO<sub>2</sub>: 268 nm, Si: 110 nm

 $d_{\text{Ge,homo}}$ : 912.5 nm

Device without a Si spacer Device with a Si spacer

metasurface, the Ge base, and the Si spacer. The structure of the device in a single metasurface period is marked within a red dashed square, and the detailed setting is illustrated on the right side of Fig. 1(b). The overall thickness of the Ge layer,  $d_{\rm Ge,hetero}$ , and that of the Si spacer,  $d_{\rm Si}$ , constitute that of the heterogeneous Ge/Si cavity. The device with the Si spacer is aimed at high-speed applications and discussed subsequently. The parameters used in this work are listed at the bottom of Fig. 1. The details of the relationship between  $d_{\rm Ge,homo}$ ,  $d_{\rm Ge,hetero}$ , and  $d_{\rm Si}$  is also discussed subsequently.

Assuming that the absorbed photons are completely converted into electrons, the quantum efficiency of a conventional RCE photodetector is expressed as [21]

$$\eta_{\text{RCE-PD}} = \frac{\left(1 + R_2 e^{-\alpha d}\right) (1 - R_1) \left(1 - e^{-\alpha d}\right)}{1 - \sqrt{R_1 R_2} e^{-\alpha d} \cos(2k n_{\text{c}} d + \varphi_1 + \varphi_2) + R_1 R_2 e^{-\alpha d}},$$
(1)

where  $R_1$  and  $R_2$  are the reflectances of the top and bottom reflectors,  $\varphi_1$  and  $\varphi_2$  are the phase shifts of the top and bottom reflectors, respectively,  $\alpha$  is the absorption coefficient, d is the thickness of the absorption layer, k is the light propagation constant in free space, and  $n_c$  is the effective refractive index of the cavity. In this equation, the thickness of the absorption layer is assumed to be equal to the cavity length. According to (1), a sufficiently large  $R_2$  and a relatively small  $R_1$  are required for a high quantum efficiency. In addition to the reflectances of reflectors, the total phase shift of light

propagation within the cavity,  $2kn_cd$ , also affects the quantum efficiency due to the interference effect.

The quantum efficiency of a RCE photodetector increases at a specific resonance wavelength with a narrow linewidth. At a specific resonance wavelength, light transmitted from the top reflector and then reflected by the bottom reflector destructively interferes with light reflected from the top reflector, resulting in optimal coupling between the incident light and the absorbing cavity. By contrast, at a non-resonance wavelength, the interference of the reflections from the two reflectors results in high overall reflectance of the incident light, leading to low coupling into the absorbing cavity.

High-reflectance reflectors ensure a strong standing wave at resonance when constructive interference occurs within the cavity. However, a large  $R_1$  allows little incident light into the cavity, thus reducing the effect of the RCE. To optimize the RCE, the amplitude of the reflection from the top reflector must be matched with that of the reflection from the bottom reflector by adjusting  $R_1$  and  $R_2$ . Although decreasing the value of  $R_1$  from that of perfect coupling broadens the linewidth at a resonance wavelength and raises the quantum efficiency at a non-resonance wavelength, the peak quantum efficiency at a resonance wavelength is reduced. This feature has been discussed in our previous work [28]. To verify the concept, we consider an extreme case that the reflectance  $R_1$  of the top reflector is near zero and the reflectance  $R_2$  of the bottom reflector is near unity. Then, (1) reduces to

$$\eta = 1 - e^{-2\alpha d}. (2)$$

This relation indicates that the quantum efficiency of the device in this case is equal to that of double-pass absorption for the device containing a top reflector with perfect antireflection coating and a bottom reflector with total reflection. In this extreme case, the quantum efficiency only weakly varies with wavelength through the wavelength dependence of the absorption coefficient  $\alpha$  because RCE is clearly absent. Indeed, for the highest peak quantum efficiency derived from RCE, the optimum value of the surface reflectance  $R_1$ depends on the value of the product  $\alpha d$  for a given value of the bottom reflectance  $R_2$ , such as its optimum value of unity. For given values of the product  $\alpha d$  and the bottom reflectance  $R_2$ , lowering the value of the surface reflectance  $R_1$  below its optimum value leads to a reduced peak quantum efficiency and a broadened resonance linewidth, thus obliterating the effect of RCE.

A nanoscale slit structure of the proposed metasurface is introduced to the device to improve the low quantum efficiency of RCE photodetectors at non-resonance wavelengths without sacrificing the high quantum efficiency at resonance wavelengths. The width of a nanoscale slit is smaller than the wavelength of the incident wave, leading to a strong diffraction effect [31]. Part of the incident wave is coupled into the device by the nanoscale slit structure. Meanwhile, the characteristics of the Ge cavity remain valid. As a result, light coupling into the absorbing cavity at a non-resonance



wavelength is improved while the high quantum efficiency at a resonance wavelength remains.

Moreover, the periodic nano-slit metasurface provides an additional phase shift of the resonance cavity. The effective refractive index of the cavity is determined by the Ge duty factor of the periodic metasurface, which is the fraction of the Ge section in a period of the nano-slit structure. Besides, scattering of the nanoscale structure offers additional phase disturbance in the metasurface. This periodic metasurface structure also facilitates phase matching, which enables incident light at a non-resonance wavelength of the vertical cavity to be coupled with the horizontal guided modes of the layers underlying the metasurface structure. Guided-mode resonance provides an additional opportunity for tailoring a broad absorbing spectrum.

#### III. THEORETICAL MODEL

## A. CALCULATION OF QUANTUM EFFICIENCY AND RESPONSIVITY

The quantum efficiency of a conventional RCE photodetector can be evaluated with (1) based on the transfer matrix method. However, (1) is not suitable for a RCE photodetector that has a structured metasurface due to the complicated thin-film interference and light diffraction. The finite element method (FEM) is used to assess the quantum efficiency of the device by calculating the steady-state electric field distribution. The responsivity is further derived with (3):

$$R = \eta \frac{q}{h\nu},\tag{3}$$

where  $\eta$  is quantum efficiency, q is the electron charge, h is the Plank constant, and  $\nu$  is the optical frequency.

A FEM model utilized in this study comprises a singleperiod unit, as shown on the right side in Fig. 1, with periodic boundaries and incorporates perfect matching layers (PMLs). This model configuration has undergone thorough verification in our previous research [32], and numerous studies have successfully adopted it. At a near-infrared spectral range of 1000-1600 nm, Si and SiO<sub>2</sub> exhibit nearly wavelengthindependent refractive indices of 3.48 and 1.45, respectively. Their extinction indices are set to 0 due to their infrared transparency. Notably, the wavelength dependence of both the refractive and the extinction indices of Ge cannot be ignored in this spectral range. The refractive index of Ge as a function of wavelength is determined from experimental data [33]. To account for the absorption enhancement resulting from the strain between Ge and Si, the extinction index of Ge as a function of wavelength is calibrated using the extracted Geon-Si absorption curve [21].

## B. BANDWIDTH

The 3-dB frequency characterizes the speed of a photodetector. It refers to the frequency at which the output electrical power is attenuated by 3 dB compared to the DC output in response to an unmodulated CW signal [34]. In this work, we utilize a vertical absorbing structure to evaluate the 3-dB

frequency of the device [34], [35]. Two factors set the limit of the speed, thus the 3-dB frequency, of a photodetector: the transit time,  $\tau_{tr}$ , of the photogenerated carriers across its active region and the RC time constant,  $\tau_{RC}$ , of its equivalent circuit [34].

For a Ge photodetector, the carrier transit time is calculated at a Ge drift saturation speed of  $6 \times 10^4$  m/s [36]. The transit-time-limited 3-dB frequency can be calculated as [34]

$$f_{\rm tr,3dB} \approx \frac{0.443}{\tau_{\rm tr}}.\tag{4}$$

The RC time constant is  $\tau_{RC} = R_L C_i$ , where  $R_L$  is the load resistance of the equivalent circuit of the photodetector and  $C_i$  is the internal capacitance of the photodetector caused by the attribution of the electric circuit, which can be calculated with (5). For a well-designed high-speed circuitry, the load resistance  $R_L$  is set at 50  $\Omega$  to match the RF impedance of a standard measurement system. The internal capacitance  $C_i$  is determined by the junction area and the thickness of the active layer, which is the intrinsic layer in the case of a PIN photodiode. The RC-time-limited 3-dB frequency can be calculated as [34]

$$f_{\rm RC,3dB} = \frac{1}{2\pi \tau_{\rm RC}} = \frac{1}{2\pi R_{\rm L} C_{\rm i}}.$$
 (5)

The overall 3-dB frequency can be calculated approximately as [35], [36]

$$f_{3dB} = (f_{tr,3dB}^{-2} + f_{RC,3dB}^{-2})^{-1/2}.$$
 (6)

## **IV. RESULTS AND DISCUSSION**

# A. DEVICE WITH A SiO<sub>2</sub>-FILLED NANO-SLIT METASURFACE FOR HIGH QUANTUM EFFICIENCY

Figures 2(a) and (b) show the quantum efficiency spectra of the device structure without a Si spacer, as shown in Fig. 1(a), for two different metasurface parameter settings, which exhibit quite different spectra. This structure has a periodic Ge/SiO<sub>2</sub> metasurface of 812.5 nm thickness on a Ge base of 100 nm thickness, resulting in  $d_{\text{Ge,homo}}$  of 912.5 nm. This value of  $d_{\text{Ge,homo}}$  is designed for a horizontally uniform plain Ge thin-film device of such thickness with an unstructured plain surface (equivalent to a Ge duty factor of 1 for the metasurface) to produce Fabry-Perot resonances near the wavelengths of 1310 nm and 1550 nm. The distinct peaks in the quantum efficiency spectrum of the thin-film device with an unstructured plain surface verify the expected Fabry-Perot resonances, as seen in the spectrum shown as the black curves in Figs. 2(a) and (b). For direct comparison, the spectra of the device with a metasurface of two different sets of structural parameters are shown as the red curves in Figs. 2(a) and (b). The spikes marked with arrows and asterisks in these spectra are respectively attributed to the Fabry-Perot resonances of the metasurface and the guided modes of the multilayer structure within the Ge metasurface and the DBR [37], [38]. The multilayers of the Ge metasurface and the DBR work as a slab waveguide in the horizontal direction. The guided modes in the multilayers are not solely confined to the Ge region

with the highest refractive index; for certain guided modes, they also penetrate the bottom DBR. Although the SiO<sub>2</sub>/Si DBR exhibits high reflectance over a broad spectral range, some diffraction modes from the metasurface couple into the waveguide modes of the DBR.

Figure 2(a) illustrates the quantum efficiency spectrum of the device with a metasurface that has a period of 2.5  $\mu$ m and a Ge duty factor of 0.7. The period is significantly larger than the wavelength of the incident light, indicating the small effect of phase shift on the Fabry-Perot modes with diffraction of the metasurface. These peaks, marked with downward arrows, indicate only small shifts of the Fabry-Perot resonance peaks to shorter wavelengths. The metasurface improves the quantum efficiency at nonresonance wavelengths of Fabry-Perot through the slit diffraction. Furthermore, the new peaks at 1426 nm and 1586 nm emerge from the phase-matched coupling of the metasurface structure to the horizontal guided modes of the Ge metasurface and the 100 nm Ge base with leakage coupling into the DBR. These relatively small peaks are marked with asterisks for clarity. These new resonances caused by the coupling of the metasurface significantly increase the quantum efficiency of the device at wavelengths away from the Fabry-Perot resonance peaks. As a result, the quantum efficiency increases from 32.91% to 59.69 at 1230 nm, from 26.56% to 49.86% at 1425 nm, and from 20.85% to 52.37% at 1586 nm. The quantum efficiency at these non-resonance wavelengths of the Fabry-Perot cavity is enhanced nearly twice by the metasurface. On average, the quantum efficiency for this structure is 61.27%, with an estimated responsivity of 0.81 A/W at 1300 nm and 0.93 A/W at 1550 nm.

Figure 2(b) illustrates the quantum efficiency of the device with a metasurface that has a period of 1  $\mu$ m and a Ge duty factor of 0.6. The period is smaller than the wavelength of the incident light, and the width of the Ge section is 600 nm. In this case, the diffraction of the metasurface causes large phase shifts in the Fabry-Perot modes, resulting in large shifts of the Fabry–Perot resonance peaks from 1168 nm to 1094 nm, from 1314 nm to 1277 nm, and from 1549 nm to 1486 nm. These resonance peaks of Fabry-Perot modes are marked with downward arrows. Multiple new resonance peaks are observed owing to the phase-matched coupling of the subwavelength metasurface structure to the horizontal guided modes with most of the field confined to the Ge metasurface and 100 nm Ge base. These peaks are observed at 1187 nm, 1383 nm, and 1552 nm in the spectrum, and are marked with asterisks. The multiple resonance peaks create a spectrum of high quantum efficiency, with an average quantum efficiency of 73.28% in the 1000-1600 nm range, covering the key application wavelengths of 1064 nm, 1310 nm, and 1550 nm. Moreover, the estimated responsivity is as high as 0.70 A/W at 1064 nm, 0.81 A/W at 1300 nm, and 1.23 A/W at 1550 nm.

As shown in Fig. 2(b), the optimized device exhibits a broad spectrum of high quantum efficiency, with a peak value

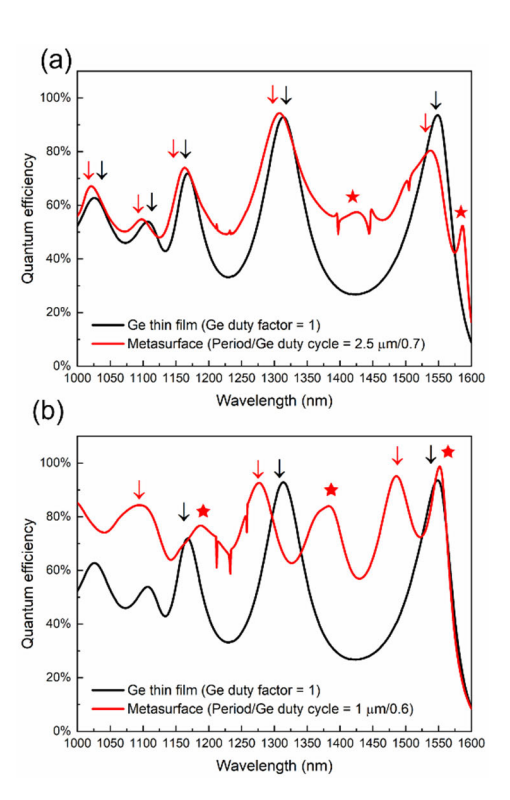


**FIGURE 2.** Quantum efficiency spectra of the device with a metasurface as shown in Fig. 1(a) for two sets of metasurface parameters: (a) a period of 2.5  $\mu$ m and a Ge duty factor of 0.7 and (b) a period of 1  $\mu$ m and a Ge duty factor of 0.6. These spectra are shown as red curves. For reference, the quantum efficiency spectrum of a horizontally uniform plain Ge thin-film device with a Ge duty factor of 1 is also plotted in black. The peaks of the Fabry-Perot modes are marked with downward arrows (\$\psi\$), and those of the guided modes involved in the multilayers are marked with asterisks (\*).

reaching 98.69% at around 1550 nm. However, several factors can lead to a decrease in quantum efficiency if they are not properly managed. The most outstanding factors are the electrical design of the device, the quality of the Ge layer, and the passivation of the surface structure.

Proper design of a metal contact is crucial to ensure an ohmic contact that maximizes the collection efficiency of the photocurrent. Additionally, the patterns of the metallic electrodes can influence the coupling of incident light to the active region, which may reduce the quantum efficiency, as observed in a RCE MSM photodetector [39]. Material defects and surface imperfections introduce additional recombination centers, further reducing the quantum efficiency. Surface structures, often fabricated through etching, can result in surface defects, making effective passivation necessary.

Achieving a high quantum efficiency in a device with a surface structure is possible despite these challenges. From [17], a device with nano-holes has achieved a high quantum efficiency of 80%, and the measurement result is close to the calculated results. It suggests that our proposed device could also maintain a high quantum efficiency in experimental settings. Thus, while the challenges are recognized, we believe



that our device has the potential to achieve near-ideal quantum efficiency in practice.

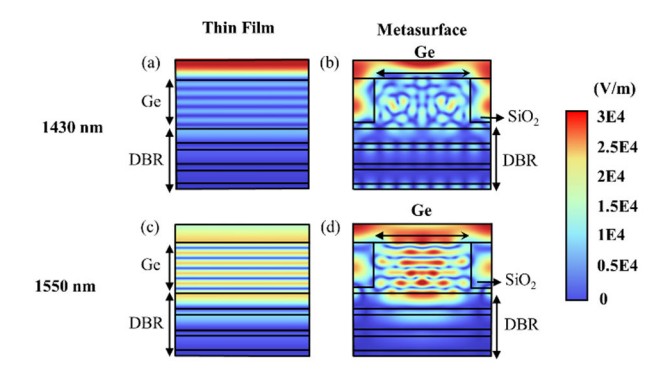


**FIGURE 3.** Comparison of the distributions of electric field amplitude in the plain thin-film device and the metasurface device at the wavelengths of (a, b) 1430 nm and (c, d) 1550 nm. The metasurface has a period of  $2.5\mu m$  and a duty factor of 0.7.

Figure 3 illustrates the distributions of the electric field amplitude at two different wavelengths in a horizontally uniform plain thin-film device and those in a single period of the metasurface device that has a period of 2.5  $\mu$ m and a Ge duty factor of 0.7. Figures 3(a) and (c) show the distributions in the plain thin-film device at 1430 nm and 1550 nm, which respectively correspond to a non-resonance and a resonance wavelength of the vertical Fabry-Perot cavity. The field amplitude in the Ge cavity at 1550 nm is much larger than that at 1430 nm, which is consistent with the spectrum shown as black curves in Fig. 2. The field amplitudes of the metasurface device at 1430 nm and 1550 nm are shown in Figs. 3(b) and (d), respectively. At 1430 nm, the field amplitude in the Ge pillar of the metasurface is significantly larger than that in the Ge layer of the thin-film device, indicating light coupling to the metasurface at the non-resonance wavelength of the Fabry-Perot cavity. At 1550 nm, the field amplitude in the Ge pillar of the metasurface device is even stronger than that in the Ge layer of the thin-film device. Although the localized electric field amplitude of the metasurface device is stronger than that of the thin-film device, the quantum efficiency of the metasurface device at this wavelength is lower than that of the thin-film device, as shown in Fig. 2(a). The lower quantum efficiency of the metasurface device can be attributed to the reduction of the Ge duty factor to 0.7 for the metasurface device from 1 for the plain thin-film device.

Vertical standing-wave patterns are observed in Figs. 3(a) and (c) resulting from wave interference in the vertical Fabry–Perot cavity of the plain thin-film device. By comparison, the electric field amplitude patterns shown in Figs. 3(b) and (d) show complicated horizontal standing-wave patterns besides vertical standing-wave patterns because of lateral diffraction caused by the metasurface structure. At the two wavelengths of 1430 nm and 1550 nm, the effect of diffraction becomes prominent in this metasurface device because the 750 nm width of the SiO<sub>2</sub>-filled nano-slit is smaller than the wavelength of the incident light.

The diffracted wave penetrates the Ge pillar from the slits on the two sides, resulting in horizontal interference in this region. The diffraction patterns at the corners of the Ge pillar are consistent with the previous research [40], highlighting the strong diffraction occurrence at the corners of the Ge pillar.

#### B. EFFECTS OF THE PARAMETERS OF THE METASURFACE

In this section, we study the effects of the metasurface parameters. We find that the width of the SiO<sub>2</sub> slit in a period affects light diffraction of the metasurface, while the width of the metasurface period determines the number of resonance peaks in a specific spectral range, as seen in Fig. 2. We also study the quantum efficiency of the device for various metasurface periods and Ge duty factors, as shown in Fig. 4. The device configuration is depicted in Fig. 1(a). We vary the Ge duty factor from 0.3 to 0.85 and the period length from 0.5  $\mu$ m to 2.5  $\mu$ m. Figures 4(a-e) show the results for period lengths ranging from subwavelength to one wavelength (from 0.5  $\mu$ m to 1.5  $\mu$ m), while Fig. 4(f) illustrates the outcome for the 2.5  $\mu$ m period, which is significantly larger than the wavelengths in the 1100–1600 nm spectral range of interest.

As shown in Fig. 4(f) for a metasurface period of 2.5  $\mu$ m, the spectrum in the range of 1000-1600 nm exhibits three distinctive peaks for a Ge duty factor larger than 0.5, which are attributed to Fabry-Perot resonances. Only small wavelength shifts caused by varying the Ge duty factor are observed for the three resonance peaks at 1150 nm, 1300 nm, and 1530 nm, while the peak values decrease as the Ge duty factor decreases. By contrast, large wavelength shifts caused by varying the Ge duty factor are observed for the resonance peaks in the spectrum of a metasurface with a subwavelength period of 0.5  $\mu$ m shown in Fig. 4(a). In this case, the period was considerably shorter than the wavelength of the incident light. As the Ge duty factor decreases, the peaks of Fabry-Perot resonances shift to shorter wavelengths, and a new resonance peak occurs at a longer wavelength that varies with the Ge duty factor. Thus, for a device with a small period length below the wavelength of the incident light, the wavelengths of the Fabry-Perot resonances are tunable with the Ge duty factor. However, the effect is not observed for a period length larger than the wavelength of the incident light.

The metasurface not only produces a shift of the peak wavelength of a Fabry-Perot resonance but also leads to the broadening of the peak, as seen in Figs. 2(a) and 4(f) of the devices with a 2.5  $\mu$ m period. The nano-slits also enhance the light coupling at the non-resonance wavelengths. The broadening effect becomes prominent when the metasurface period is less than 1.5  $\mu$ m, such as at a small Ge duty factor of 0.4 for the 1- $\mu$ m period. The resonance peaks split and overlap, as seen in Fig. 4(c), and additional peaks can be observed between the Fabry-Perot peaks. These additional peaks arise from the phase-matched coupling of the incident to the horizontal guided modes in the periodic metasurface. For a period in the range of 0.8  $\mu$ m to 1.5  $\mu$ m, a broad spectrum of high quantum efficiency is observed for a Ge

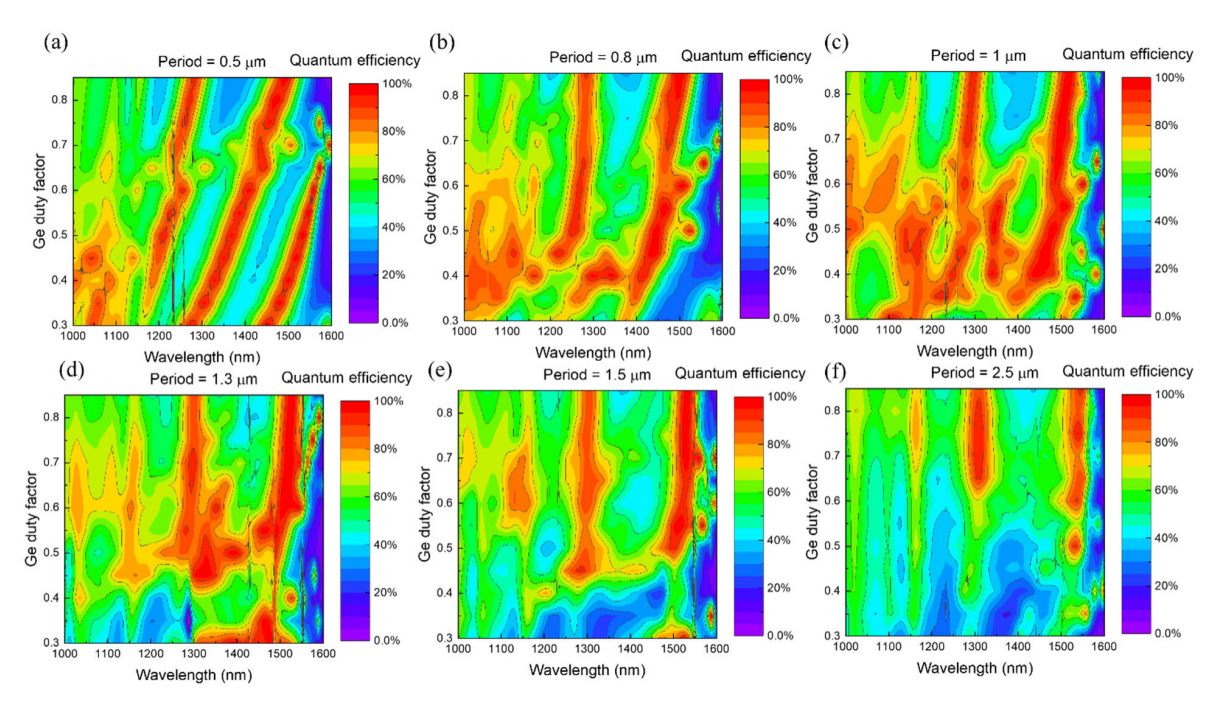
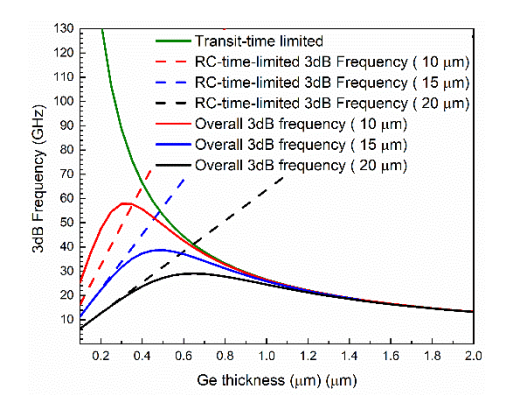


FIGURE 4. Quantum efficiency of the metasurface device as a function of the Ge duty factor and the wavelength of the incident light for various period lengths of the metasurface. (a) Period =  $0.5 \mu$ m. (b) Period =  $0.8 \mu$ m. (c) Period =  $1.4 \mu$ m. (d) Period =  $1.3 \mu$ m. (e) Period =  $1.5 \mu$ m. (f) Period =  $1.5 \mu$ m.

duty factor around 0.4, as seen in Figs. 2(a)-(e). By contrast, such a continuous spectrum is not observed in Fig. 2(a), which indicates less phased-matched coupling to the horizontal waveguide modes from the metasurface in the spectral range of 1000-1600 nm

## C. DEVICE WITH A SPACER FOR HIGH-SPEED APPLICATIONS

Figure 5 illustrates how the thickness of the active layer affects the calculated 3-dB bandwidth (BW). The overall 3dB BW is influenced by two factors: the transit time and the RC delay time. A thicker active layer results in a smaller BW because it takes a longer time for the electrons and holes to travel across the device. However, a thicker active layer also means a smaller capacitance, thus a smaller RC time constant. Therefore, the optimized thickness of the active layer involves a trade-off between the transit time and the RC time. The dimensions of the device also affect the capacitance of the device. A larger device area leads to a larger capacitance, thus a larger RC time that limits the BW. For example, a device with a 10-μm diameter has a maximum overall 3-dB BW of 57.8 GHz. However, it reduces to 37.8 GHz and 28 GHz for devices with diameters of 15  $\mu$ m and 20  $\mu$ m, respectively. An effective design for a high-speed photodetector entails a small diameter and an optimally thin active layer. As the device diameter decreases, the optimum thickness of the active layer also decreases. The optimum thicknesses of the active layer are 0.35, 0.5, and 0.65  $\mu$ m for device diameters of 10, 15, and 20  $\mu$ m, respectively.



**FIGURE 5.** Calculation of the 3-dB frequency for the device shown in Fig. 1(a) as a function of the thickness of the active layer for three different device diameters of 10, 15, and 25 $\mu$ m.

In previous sections, we analyze the device shown in Fig. 1(a), the thickness of the Ge photodetector is the same as that of the cavity. However, the thickness of the active layer affects the device speed as shown in Fig. 5. Therefore, we propose a device, as shown in Fig. 1(b), that uses a high-speed Ge photodetector with a Ge/Si heterogeneous cavity and a metasurface to improve its performance. The metasurface is placed on top of a 100 nm Ge base located underneath for current extraction. The  $d_{\rm Ge,hetero}$ , is chosen to be sufficiently small to create a high-speed Ge photodetector. A Si spacer is placed underneath the Ge base layer to match the Fabry–Perot resonance. Since the refractive index of Si is similar to that of Ge, the reflectance and phase change of the interface between Ge and Si are not significant. We design the heterogeneous



Ge/Si cavity using the relation:

$$n_{\text{Ge}}d_{\text{Ge,homo}} = n_{\text{Ge}}d_{\text{Ge,hetero}} + n_{\text{Si}}d_{\text{Si}}.$$
 (7)

Equation 7 shows the relationship of the light phase between the homogeneous Ge cavity and the heterogeneous Ge/Si cavity without considering the metasurface. In the equation,  $n_{\text{Ge}}$  and  $n_{\text{Si}}$  are the refractive indices of Ge and Si, respectively,  $d_{\text{Ge,homo}}$  is the thickness of the homogeneous Ge cavity, and  $d_{\text{Ge,hetero,}}$  and  $d_{\text{Si}}$  are respectively the thicknesses of the Ge layer and Si spacer in the heterogeneous Ge/Si cavity. Moreover,  $d_{\text{Ge,homo}}$ ,  $d_{\text{Ge,hetero,}}$  and  $d_{\text{Si}}$  have been defined on the right sides of Fig.1 (a) and (b).

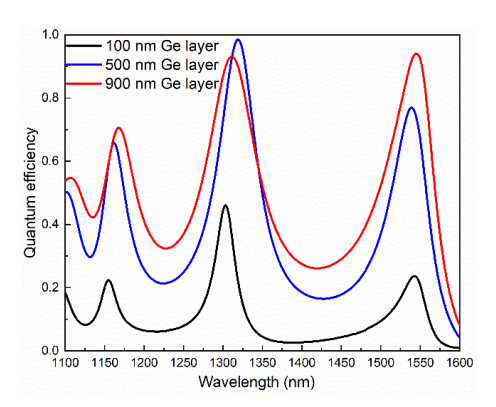


**FIGURE 6.** Quantum-efficiency spectra of thin-film devices with a Si spacer for three different thicknesses of the Ge base layer. The thickness of the Si spacer is designed with (7), in which the original Ge thickness is 912.5 nm, and the Ge thickness of the heterogeneous cavity,  $d_{\rm Ge\, hetero}$  is varied from 100 nm to 500 nm and 900 nm.

Figure 6 displays the quantum-efficiency spectra of horizontally uniform plain thin-film devices with a bottom Si spacer. The values of  $d_{\text{Ge,hetero}}$  considered in this figure are 100, 500, and 900 nm, while the thickness of the Si spacer is determined using (7). By incorporating the Si spacer, a homogeneous Ge cavity with a thickness of 912.5 nm considered in earlier sections and subsections is transformed into a heterogeneous Ge/Si cavity. The resonance wavelengths of the devices with the heterogeneous Ge/Si cavity are around 1150 nm, 1310 nm, and 1550 nm, which are in line with those of the device with the homogeneous Ge cavity. These results indicate that the approximation of (7) is appropriate.

To optimize the quantum efficiency with the thin-film Ge cavity, one must consider two factors: The first is the Ge single-pass absorption, and the other one is the resonant interference within the cavity. As seen in Fig. 6, for the resonance peak at around 1150 nm, the quantum efficiency increases with the thickness of the Ge layer. The peaks near 1150 nm are lower than the corresponding peaks near 1310 nm and 1550 nm because of the high single-pass absorption at this short wavelength, which reduces the reflected light from the bottom reflector. The consequence is a decrease in the effect of constructive interference in the cavity such that the RCE is not effective at this wavelength. By contrast, the Ge absorption coefficient drops abruptly at a wavelength around 1550 nm. Therefore, the effect of the RCE is more effective

at 1550 nm, resulting in dramatic increases of the quantum efficiency as the thickness of the absorbing Ge layer increased to 500 nm and further to 900 nm. At wavelengths close to 1300 nm, the peak quantum efficiency increases as the thickness of the absorbing Ge layer increases from 100 nm to 500 nm, but it decreases slightly as the thickness of the Ge layer further increases to 900 nm.

After analyzing the calculated data presented in Figs. 5 and 6, we can determine the optimum thickness of the active layer for the device. For this purpose, we consider a device with a diameter of  $10~\mu m$ , as it provides a high 3-dB BW. In this case, the optimum thickness of the active layer is found to be 400 nm. Considering that the thickness of the active layer is equal to or a little smaller than that of the Ge layer depending on the type of photodetector,  $d_{\rm Ge,hetero}$  is set as 600 nm. Based on (7),  $d_{\rm Si}$  for this device structure is found to be 386 nm.

Figures 7(a) and (b) illustrate the quantum efficiency of the metasurface device with a Si spacer shown in Fig. 1(b) as a function of the Ge duty factor and the wavelength of the incident light for metasurface period lengths of 1  $\mu$ m and 1.5  $\mu$ m, respectively. Compared to those shown in Figs. 4(c) and (e) for the device without a Si spacer shown in Fig. 1(a), the resonance peaks seen in Figs. 7(a) and (b) for the devices with a Si spacer exhibit narrower linewidths. The device with the Si spacer had a thin Ge layer, which was associated with low single-pass absorbance. Consequently, the quantum efficiency of the device with a Si spacer is lower than that of the device without a Si spacer at non-resonance wavelengths.

The thickness of the metasurface is noted to influence the guided mode of the Ge region. In addition, the resonance band patterns of the device with the Si spacer differed from those of the device without the Si spacer. As indicated in Fig. 7(a), for a device with a Si spacer and a Ge duty factor of 0.6, the resonance peak of the guided mode is close to and partially overlapped with the Fabry–Perot mode peak at approximately 1300 nm. By contrast, as depicted in Fig. 4(c), at the same Ge duty factor, the resonance peak for the device without a Si spacer is located at approximately 1383 nm between the two Fabry-Perot mode peaks near 1300 and 1500 nm. This discrepancy is more pronounced at a smaller Ge duty factor, where multi-resonance peaks of guided modes appeared. As shown in Fig. 4(c), at a Ge duty factor of 0.35, the peaks of the guided modes are observed at approximately 1330 and 1530 nm. As illustrated in Fig. 7(a), at a Ge duty factor of 0.4, only one peak of the guided mode is observed at 1330 nm. The guided mode is influenced by the construction of the metasurface, with the guided-mode resonance wavelength abruptly changing when a thinner metasurface and a lower Ge duty factor are used. At a period length of 1.5  $\mu$ m, the results for the device with the Si spacer in Fig. 7(b) differ from those for the device without the Si spacer in Fig. 4(e).

Figure 7(c) illustrates two detailed spectra of the quantum efficiency of the metasurface device with a Si spacer for two different sets of metasurface parameters. The upper spectrum represents a device with a 1  $\mu$ m metasurface period and a

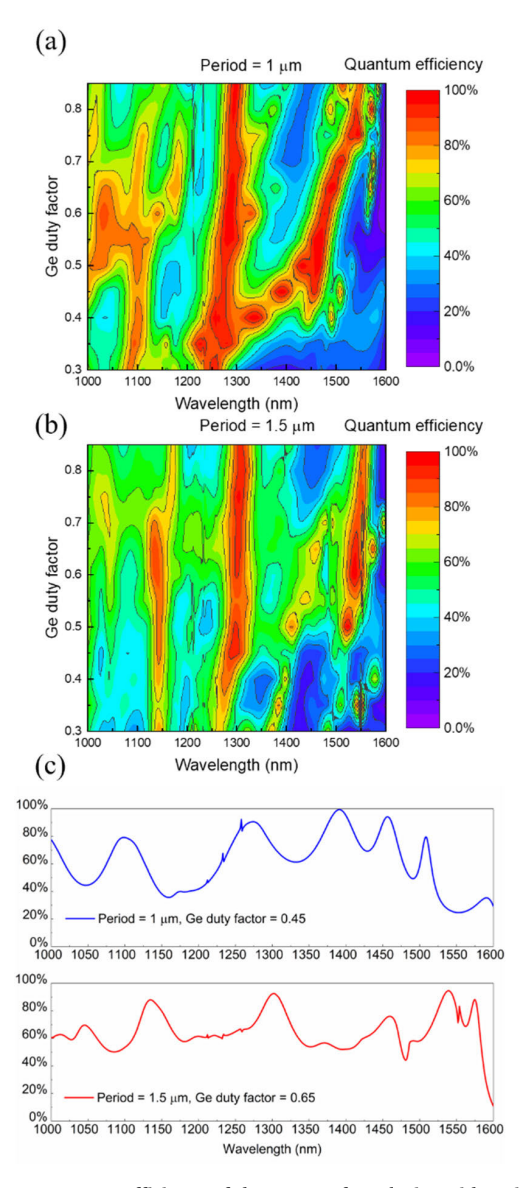


**FIGURE 7.** Quantum efficiency of the metasurface device with a Si spacer shown in Fig. 1(b) as a function of the Ge duty factor and the wavelength of the incident light for two metasurface period lengths of (a)  $1\mu$ m and (b)  $1.5\mu$ m. (c) Detailed spectra of quantum efficiency for two different sets of parameters for the metasurface grating.

0.45 Ge duty factor. It shows a significant quantum efficiency in the spectral range of  $1250{\text -}1520$  nm, with four adjacent peaks over 80% quantum efficiency. The lower spectrum represents a device with a  $1.5{\text -}\mu\text{m}$  metasurface period and a 0.65 Ge duty factor. Although the peaks in this spectrum are less pronounced and thus appear to be more separated than those in the upper spectrum, the overall quantum efficiency of the spectrum is still around 60%.

The device with a 1  $\mu$ m period exhibits a high quantum efficiency with four adjacent peaks across a broad spectral range from 1250 nm to 1520 nm, but its quantum efficiency at 1550 nm is drastically reduced. By contrast, the device with a 1.5  $\mu$ m period exhibits a high quantum efficiency at 1300 nm, 1450 nm, and 1550 nm, effectively covering the

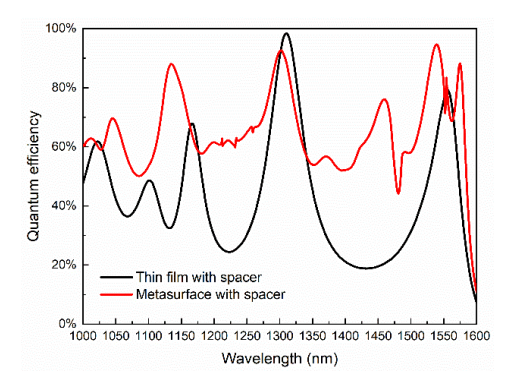


**FIGURE 8.** Quantum efficiency spectra of the metasurface device and the plain thin-film device with 600 nm Ge thickness (Period/Ge duty factor =  $1.5\mu$ m/0.65). Both devices have a Si spacer.

primary wavelengths relevant to major infrared applications, such as optical communications.

A comparison between devices with and without a metasurface is presented in Fig. 8. The period is chosen to be 1.5  $\mu$ m, and the Ge duty factor is 0.65. Both devices have a bottom Si spacer that has a thickness of 386 nm. The metasurface device shows a high quantum efficiency over a broad spectral range, which is supported by previous results obtained from devices without a Si spacer (refer to Fig. 2). The peak values of the spectrum of the metasurface device are comparable to those of the plain thin-film device. Additionally, the valley values of the spectrum of the metasurface device are three times those of the plain thin-film device. The peak quantum efficiency of the metasurface photodetector reaches 92.61% at around 1300 nm and 94.65% at around 1550 nm, with the corresponding estimated responsivity being 0.98 A/W and 1.18 A/W, respectively. The average quantum efficiency reaches 64.96% in the range of 1000-1600 nm with only a 600-nm Ge layer, which makes it suitable for high-speed infrared photodetection applications.

As shown in the red curve of Fig. 8, the optimized device with a Si spacer demonstrates a lower average quantum efficiency of 64.96%. In contrast, the optimized device without a Si spacer shows a higher average quantum efficiency of 73.28% as illustrated in the red curve of Fig. 2(b). This reduction is primarily attributed to the decreased absorption at non-resonance wavelengths, which is a result of the thinner Ge layer in the configuration with a Si spacer. Despite this difference, both designs achieve comparable quantum efficiencies at the resonance wavelength. It is worth noting that the BW of the optimized device with a Si spacer is twice that of the device without the spacer. Therefore, depending on the intended application, the Si spacer design is more suitable for ultra-high-speed detection, whereas the design without the Si spacer is better optimized for broadband detection.

### **V. CONCLUSION**

We have proposed a new design of Ge-on-Si RCE photodetectors to achieve high quantum efficiency for broadband infrared sensing applications. This is done by creating a metasurface of nano SiO<sub>2</sub>-filled slits on a free-standing RCE



Ge structure, which demonstrates high quantum efficiency in a broad spectral range of 1000-1600 nm. The design overcomes the distinct drawback of conventional RCE devices, which have narrow linewidths due to the limitations of the Fabry-Perot cavity. Light diffraction of the SiO<sub>2</sub>-filled nanoscale metasurface improves the light coupling to the absorbing Ge region at non-resonance wavelengths. Furthermore, the additional phase shift caused by the slit scattering introduces new resonances at non-resonance wavelengths of the Fabry-Perot cavity through phase-matched coupling with the horizontal guided modes. The optimized device exhibits a 73.48% average quantum efficiency in the spectral range of 1000–1600 nm. The quantum efficiency at around 1300 nm and around 1550 nm reaches 76.65% and 98.69%, respectively, for a device with a Ge layer of 912.5 nm thickness. Even at 1430 nm, the minimum quantum efficiency is 60%, which is three times that of the plain thin-film device. The estimated responsivity is as high as 0.70 A/W at 1064 nm, 0.81 A/W at 1300 nm, and 1.23 A/W at 1550 nm. To enhance the response speed, a device with a Si spacer is designed for a 55 GHz bandwidth. With a Ge layer of 600 nm thickness, the device exhibits a 64.96% average quantum efficiency in the spectral range of 1000-1600 nm. The peak quantum efficiency of the metasurface photodetector reaches 92.61% at around 1300 nm and 94.65% at around 1550 nm, with the corresponding estimated responsivity being 0.98 A/W and 1.18 A/W, respectively. This design paves the way for highspeed infrared photodetectors of high quantum efficiency over a broad spectral range that is needed in a wide range of fields, including telecommunications, sensing, and imaging, where precise and efficient infrared photodetection is essential.

#### **REFERENCES**

- V. Sorianello, A. Perna, L. Colace, G. Assanto, H. C. Luan, and L. C. Kimerling, "Near-infrared absorption of germanium thin films on silicon," *Appl. Phys. Lett.*, vol. 93, no. 11, Sep. 2008, Art. no. 111115.
- [2] J. Joo, S. Kim, I. G. Kim, K.-S. Jang, and G. Kim, "High-sensitivity 10 Gbps Ge-on-Si photoreceiver operating at  $\lambda \sim 1.55~\mu$ m," *Opt. Exp.*, vol. 18, no. 16, pp. 16474–16479, 2010.
- [3] J. Osmond, L. Vivien, J.-M. Fédéli, D. Marris-Morini, P. Crozat, J.-F. Damlencourt, E. Cassan, and Y. Lecunff, "40 Gb/s surfaceilluminated Ge-on-Si photodetectors," *Appl. Phys. Lett.*, vol. 95, no. 15, Oct. 2009, Art. no. 151116.
- [4] S. Lischke, A. Peczek, J. S. Morgan, K. Sun, D. Steckler, Y. Yamamoto, F. Korndörfer, C. Mai, S. Marschmeyer, M. Fraschke, A. Krüger, A. Beling, and L. Zimmermann, "Ultra-fast germanium photodiode with 3-dB bandwidth of 265 GHz," *Nature Photon.*, vol. 15, no. 12, pp. 925–931, Dec. 2021.
- [5] Y. Li and J. Ibanez-Guzman, "LiDAR for autonomous driving: The principles, challenges, and trends for automotive LiDAR and perception systems," *IEEE Signal Process. Mag.*, vol. 37, no. 4, pp. 50–61, Jul. 2020.
- [6] B. Gao, A. C. Walhof, D. A. Laird, F. Toor, and J. P. Prineas, "Analytical evaluation of mobile in situ soil nitrate infrared sensor designs for precision agriculture," *IEEE Sensors J.*, vol. 21, no. 18, pp. 20200–20209, Sep. 2021.
- [7] T. P. Wrobel and R. Bhargava, "Infrared spectroscopic imaging advances as an analytical technology for biomedical sciences," *Anal. Chem.*, vol. 90, no. 3, pp. 1444–1463, Feb. 2018.
- [8] E. El-Fiky, M. Osman, A. Samani, C. Gamache, M. H. Ayliffe, J. Li, M. Jacques, Y. Wang, A. Kumar, and D. V. Plant, "First demonstration of a 400 Gb/s 4λ CWDM TOSA for datacenter optical interconnects," *Opt. Exp.*, vol. 26, no. 16, pp. 19742–19749, 2018.

- [9] A. M. Lines, G. B. Hall, S. Asmussen, J. Allred, S. Sinkov, F. Heller, N. Gallagher, G. J. Lumetta, and S. A. Bryan, "Sensor fusion: Comprehensive real-time, on-line monitoring for process control via visible, near-infrared, and Raman spectroscopy," ACS Sensors, vol. 5, no. 8, pp. 2467–2475, Aug. 2020.
- [10] J. Michel, J. Liu, and L. C. Kimerling, "High-performance Ge-on-Si photodetectors," *Nature Photon.*, vol. 4, no. 8, pp. 527–534, Aug. 2010.
- [11] M. Halbwax, M. Rouviere, Y. Zheng, D. Debarre, L. H. Nguyen, J.-L. Cercus, C. Clerc, V. Yam, S. Laval, E. Cassan, and D. Bouchier, "UHV-CVD growth and annealing of thin fully relaxed Ge films on (001)Si," *Opt. Mater.*, vol. 27, no. 5, pp. 822–826, Feb. 2005.
- [12] J. Vanjaria, A. C. Arjunan, Y. Wu, G. S. Tompa, and H. Yu, "Epitaxial Ge thin film growth on Si using a cost-effective process in simplified CVD reactor," ECS J. Solid State Sci. Technol., vol. 9, no. 3, Mar. 2020, Art. no. 034008.
- [13] J. Liu, H. J. Kim, O. Hul'ko, Y. H. Xie, S. Sahni, P. Bandaru, and E. Yablonovitch, "Ge films grown on Si substrates by molecular-beam epitaxy below 450°C," J. Appl. Phys., vol. 96, no. 1, pp. 916–918, Jul. 2004.
- [14] D. Benedikovic, L. Virot, G. Aubin, J.-M. Hartmann, F. Amar, X. L. Roux, C. Alonso-Ramos, É. Cassan, D. Marris-Morini, F. Boeuf, J.-M. Fédéli, B. Szelag, and L. Vivien, "Silicon-germanium avalanche receivers with fJ/bit energy consumption," *IEEE J. Sel. Topics Quantum Electron.*, vol. 28, no. 2, pp. 1–8, Mar. 2022.
- [15] C.-H. Lin, D.-W. Huang, T.-T. Shih, H.-C. Kuo, and S.-W. Chang, "Increasing responsivity-bandwidth margin of germanium waveguide photodetector with simple corner reflector," *Opt. Exp.*, vol. 29, no. 7, pp. 10364–10373, 2021.
- [16] A. Beling and J. C. Campbell, "High-speed photodiodes," *IEEE J. Sel. Topics Quantum Electron.*, vol. 20, no. 6, pp. 57–63, Nov. 2014.
- [17] H. Cansizoglu, C. Bartolo-Perez, Y. Gao, E. P. Devine, S. Ghandiparsi, K. G. Polat, H. H. Mamtaz, T. Yamada, A. F. Elrefaie, S.-Y. Wang, and M. S. Islam, "Surface-illuminated photon-trapping high-speed Ge-on-Si photodiodes with improved efficiency up to 1700 nm," *Photon. Res.*, vol. 6, no. 7, pp. 734–742, 2018.
- [18] B. Son, H. Zhou, Y. Lin, K. H. Lee, and C. S. Tan, "Gourd-shaped hole array germanium (Ge)-on-insulator photodiodes with improved responsivity and specific detectivity at 1,550 nm," *Opt. Exp.*, vol. 29, no. 11, pp. 16520–16533, 2021.
- [19] A. Y. Zhu, S. Zhu, and G.-Q. Lo, "Guided mode resonance enabled ultra-compact germanium photodetector for 1.55  $\mu$ m detection," *Opt. Exp.*, vol. 22, no. 3, pp. 2247–2258, 2014.
- [20] Z. Liu, J. Liu, B. Cheng, J. Zheng, C. Li, C. Xue, and Q. Wang, "Enhanced light trapping in Ge-on-Si-on-insulator photodetector by guided mode resonance effect," *J. Appl. Phys.*, vol. 124, no. 5, Aug. 2018, Art. no. 053101.
- [21] O. I. Dosunmu, D. D. Cannon, M. K. Emsley, B. Ghyselen, J. Liu, L. C. Kimerling, and M. S. Unlu, "Resonant cavity enhanced Ge photodetectors for 1550 nm operation on reflecting Si substrates," *IEEE J. Sel. Topics Quantum Electron.*, vol. 10, no. 4, pp. 694–701, Aug. 2004.
- [22] O. I. Dosunmu, D. D. Cannon, M. K. Emsley, L. C. Kimerling, and M. S. Unlu, "High-speed resonant cavity enhanced Ge photodetectors on reflecting Si substrates for 1550-nm operation," *IEEE Photon. Technol. Lett.*, vol. 17, no. 1, pp. 175–177, Jan. 1, 2005.
- [23] S. Ghosh, K.-C. Lin, C.-H. Tsai, K. H. Lee, Q. Chen, B. Son, B. Mukhopadhyay, C. S. Tan, and G.-E. Chang, "Resonant-cavityenhanced responsivity in germanium-on-insulator photodetectors," *Opt. Exp.*, vol. 28, no. 16, p. 23739, 2020.
- [24] C. B. Li, R. W. Mao, Y. H. Zuo, L. Zhao, W. H. Shi, L. P. Luo, B. W. Cheng, J. Z. Yu, and Q. M. Wang, "1.55 μm Ge islands resonant-cavity-enhanced detector with high-reflectivity bottom mirror," *Appl. Phys. Lett.*, vol. 85, no. 14, pp. 2697–2699, Oct. 2004.
- [25] T. Yezekyan, V. A. Zenin, M. Thomaschewski, R. Malureanu, and S. I. Bozhevolnyi, "Germanium metasurface assisted broadband detectors," *Nanophotonics*, vol. 12, no. 12, pp. 2171–2177, Jun. 2023.
- [26] L. Wang, Y. Zhang, B. Wang, Y. Wei, B. Zhang, L. Meng, T. Liu, B. Wang, B. Han, Z. Jiang, and H. Hu, "High-performance infrared Gebased plasmonic photodetector enhanced by dual absorption mechanism," *APL Photon.*, vol. 5, no. 9, Sep. 2020, Art. no. 096104.
- [27] L. Tang, S. E. Kocabas, S. Latif, A. K. Okyay, D.-S. Ly-Gagnon, K. C. Saraswat, and D. A. B. Miller, "Nanometre-scale germanium photodetector enhanced by a near-infrared dipole antenna," *Nature Photon.*, vol. 2, no. 4, pp. 226–229, Apr. 2008.



- [28] C.-Y. Hsu, Z. Pei, and J.-M. Liu, "High-absorbance resonant-cavity-enhanced free-standing Ge photodetector for infrared detection at 1550 nm wavelength," AIP Adv., vol. 13, no. 7, Jul. 2023, Art. no. 075006.
- [29] C. Zeng, H. Lu, D. Mao, Y. Du, H. Hua, W. Zhao, and J. Zhao, "Grapheneempowered dynamic metasurfaces and metadevices," *Opto-Electron. Adv.*, vol. 5, no. 4, 2022, Art. no. 200098.
- [30] D. Kang, H. Heo, Y. Yang, J. Seong, H. Kim, J. Kim, and J. Rho, "Liquid crystal-integrated metasurfaces for an active photonic platform," *Opto-Electron. Adv.*, vol. 7, no. 6, 2024, Art. no. 230216.
- [31] S. Yan, Y. Zuo, S. Xiao, L. K. Oxenløwe, and Y. Ding, "Graphene photodetector employing double slot structure with enhanced responsivity and large bandwidth," *Opto-Electron. Adv.*, vol. 5, no. 12, 2022, Art. no. 210159.
- [32] C.-Y. Hsu, Z. Pei, and J.-M. Liu, "Germanium infrared photodetector structure with Ge/SiO<sub>2</sub> grating and distributed Bragg reflector for wideangle and high response," Opt. Quantum Electron., vol. 55, no. 6, p. 526, Jun. 2023.
- [33] T. N. Nunley, N. S. Fernando, N. Samarasingha, J. M. Moya, C. M. Nelson, A. A. Medina, and S. Zollner, "Optical constants of germanium and thermally grown germanium dioxide from 0.5 to 6.6 eV via a multisample ellipsometry investigation," J. Vac. Sci. Technol. B, Nanotechnol. Microelectron., Mater., Process., Meas., Phenomena, vol. 34, no. 6, Nov. 2016, Art. no. 061205.
- [34] J.-M. Liu, Photonic Devices. Cambridge, U.K.: Cambridge Univ. Press, 2005.
- [35] K. Li, Z. Li, X. Duan, W. Yuan, Y. Li, K. Liu, and Y. Huang, "Design of a high-speed PIN photodiode with a gradually-doped composite absorption layer for 100 Gbit/s optical receivers," *IEEE J. Quantum Electron.*, vol. 58, no. 6, pp. 1–8, Dec. 2022.
- [36] S. Ghosh, B. Mukhopadhyay, and G.-E. Chang, "Design and analysis of GeSn-based resonant-cavity-enhanced photodetectors for optical communication applications," *IEEE Sensors J.*, vol. 20, no. 14, pp. 7801–7809, Jul. 2020.
- [37] W. Jian-Peng, J. Yun-Xia, M. Jian-Yong, S. Jian-Da, and F. Zheng-Xiu, "Study on guided-mode resonance characteristic of multilayer dielectric grating with broadband and wide using-angle," *Chin. Phys. B*, vol. 19, no. 5, May 2010, Art. no. 054202.
- [38] S. B. Lee, H. S. Bark, and T.-I. Jeon, "Enhancement of THz resonance using a multilayer slab waveguide for a guided-mode resonance filter," Opt. Exp., vol. 27, no. 20, pp. 29357–29366, 2019.
- [39] M. Cho, J.-H. Seo, M. Kim, J. Lee, D. Liu, W. Zhou, Z. Yu, and Z. Ma, "Resonant cavity germanium photodetector via stacked single-crystalline nanomembranes," J. Vac. Sci. Technol. B, Nanotechnol. Microelectron., Mater., Process., Meas., Phenomena, vol. 34, no. 4, Jul. 2016, Art. no. 040604.
- [40] K. C. Balram, R. M. Audet, and D. A. B. Miller, "Nanoscale resonant-cavity-enhanced germanium photodetectors with lithographically defined spectral response for improved performance at telecommunications wavelengths," Opt. Exp., vol. 21, no. 8, pp. 10228–10233, 2013.

**CHING-YU HSU** (Graduate Student Member, IEEE) received the B.S. and M.S. degrees in electrical engineering from National Chung Hsing University, Taiwan, in 2020 and 2022, respectively. He is currently pursuing the Ph.D. degree with the College of Photonics, National Yang Ming Chiao Tung University, Tainan, Taiwan. His current research interests include Ge-on-Si infrared photodetectors, dielectric gratings, and resonance cavity enhancement devices.

**ZINGWAY PEI** (Senior Member, IEEE) received the B.S. degree in physics from National Cheng Kung University, Taiwan, in 1994, and the Ph.D. degree in electrical engineering from National Tsing Hua University, Taiwan, in 2004, in the field of silicon quantum dots-based light-emitting diode and resonant transport.

In 2000, he joined the Electronic Research and Service Organization (ERSO), Industrial Technology and Research Institute (ITRI), Hsinchu, Taiwan. He worked with the microelectronic group developing advanced technology, including metal gate, high-k gate dielectric, strained-Si MOS-FET, and advance SiGe hetero-junction bipolar transistor. In 2003, he joined the flexible electronic group to develop organic based electronic and optoelectronic devices. He joined the Graduate Institute of Optoelectronic Engineering and the Department of Electrical Engineering, National Chung Hsing University, Taichung, Taiwan, in 2006. He is currently a Distinguished Professor with the Graduate Institute of Optoelectronic Engineering, National Chung Hsing University. His main research interests include applying low-dimensional materials for photovoltaic, biochemical sensors, thin-film transistors, photodetectors, and light-emitting diodes.

Dr. Pei is a Senior Member of the IEEE Electron Device Society and the IEEE Photonic Society, and a member of SPIE and Optica. He received the Outstanding Young Investigator Award from National Chung Hsing University, in 2008, the Pan Wen Yuan Foundation Exploration Research Award, in 2009, and the Excellent General Education Teaching Award from National Chung Hsing University, in 2018. He also served as the Program Chair of the 2019 Optics and Photonics Taiwan and the International Conference (OPTIC 2019).

**JIA-MING LIU** (Fellow, IEEE) received the B.S. degree in electrophysics from National Chiao Tung University, Hsinchu, Taiwan, in 1975, and the S.M. and Ph.D. degrees in applied physics from Harvard University, in 1979 and 1982, respectively.

He is currently the Northrop Grumman Distinguished Professor of electrical and computer engineering with the University of California at Los Angeles. He became a Licensed Professional Electrical Engineer, in 1977. He has published more than 250 scientific articles and 14 book chapters. He holds 12 U.S. patents. He coedited the book: *Digital Communications Using Chaos and Nonlinear Dynamics*, (Springer, 2006), and has authored four books: *Photonic Devices*, (Cambridge University Press, 2005), *Principles of Photonics*, (Cambridge University Press, 2016), *Graphene Photonics*, (Cambridge University Press, 2019), and *Nonlinear Photonics*, (Cambridge University Press, 2022). He has delivered more than 200 conference presentations and technical seminars, including more than 100 invited talks. His research interests and experiences include nonlinear optics, ultrafast optics, ultrafast dynamics, laser dynamics, semiconductor lasers, fiber lasers, photonic devices, microwave photonics, graphene photonics, nanophotonics, and supercontinuum spectroscopy.

Dr. Liu is a fellow of Optica, the American Physical Society, and the Guggenheim Foundation. He received the Quantum Electronics Award from the IEEE Photonics Society, in 2017.

• • •